On the Buckling of Elastic Rings by External Confinement

DOI:
10.1098/rsta.2016.0227

Document Version
Accepted author manuscript

PHILOSOPHICAL TRANSACTIONS A

On the Buckling of Elastic Rings by External Confinement

Journal:	*Philosophical Transactions A*
Manuscript ID	RSTA-2016-0227.R1
Article Type:	Research
Date Submitted by the Author:	n/a
Complete List of Authors:	Hazel, Andrew; University of Manchester, School of Mathematics Mullin, Tom; University of Oxford
Issue Code: Click here to find the code for your issue.:	PATTERNS
Subject:	Applied mathematics < MATHEMATICS, Mechanics < PHYSICS
Keywords:	Confined Elastic Buckling, Instability

rsta.royalsocietypublishing.org

Research

Article submitted to journal

Keywords:
Confined Elastic Buckling, Instability

Author for correspondence:
Tom Mullin
e-mail: Tom.Mullin@maths.ox.ac.uk

On the Buckling of Elastic Rings by External Confinement

Andrew L. Hazel[1] and Tom Mullin[2]

[1] School of Mathematics & Manchester Centre for Nonlinear Dynamics, University of Manchester, Oxford Road, Manchester, M13 9PL, U.K.
[2] Mathematical Institute, University of Oxford, Radcliffe Observatory, Woodstock Road, Oxford, OX2 6GG

We report the results of an experimental and numerical investigation into the buckling of thin elastic rings confined within containers of circular or regular polygonal cross section. The rings float on the surface of water held in the container and controlled removal of the fluid increases the confinement of the ring. The increased compressive forces can cause the ring to buckle into a variety of shapes. For the circular container finite perturbations are required to induce buckling, whereas in polygonal containers the buckling occurs through a linear instability that is closely related to the canonical Euler column buckling. A model based on Kirchhoff–Love beam theory is developed and solved numerically, showing good agreement with the experiments and revealing that in polygons increasing the number of sides means that buckling occurs at reduced levels of confinement.

1. Introduction

It is well known that thin-walled elastic rings, beams and tubes are prone to buckling instabilities when under compressive loads [1,2]. Elastic buckling was classically explored by Euler [3] for beams and explicit expressions for the critical compressive conditions are given in the textbook by Timoshenko and Gere [4]. The instability is a consequence of it being energetically more favourable for the structure to bend (change its curvature) so that the applied load can be balanced without increasing the in-plane stresses. The phenomenon is commonplace and has a wide range of applications in civil engineering and the safety of large-scale man-made structures [5].

In addition, elastic buckling is important in biological systems including the behaviour of cellular solids [6], the collapse and reopening of small airways [7], and flagellar hydrodynamics [8].

If an elastic ring of undeformed radius R is loaded by a uniform external pressure, assuming zero constant internal pressure, then the classic linear stability analysis, *e. g.* [9,10] shows that it will buckle when the critical load exceeds

$$P_{ext} = \frac{E}{1-\nu^2}\,\frac{1}{12}\left(\frac{h}{R}\right)^3\left[N^2-1\right], \tag{1.1}$$

where E is the Young's modulus and ν is the Poisson ratio of the ring; h is the thickness of the ring and N is an azimuthal wave number of the buckling mode. Recently, Putelat and Triantafyllidis [10] generalised the classic static stability approach to include the effects of dynamic loading, such as impact, on elastic rings.

In standard quasistatic loading, the buckling takes place as a series of supercritical pitchfork bifurcations that break the rotational symmetry of the original ring and leave conjugate solution branches of a particular azimuthal mode number N. The smallest value of P_{ext} occurs when $N = 2$, so the ring will buckle into a two-lobed mode, as commonly observed. However, buckling into higher modes is possible for higher external pressures, see Figure 1 for postbuckling curves when $N = 2$ and $N = 3$. In every case the post-buckling shapes have regions that protrude beyond the boundary of the original undeformed ring.

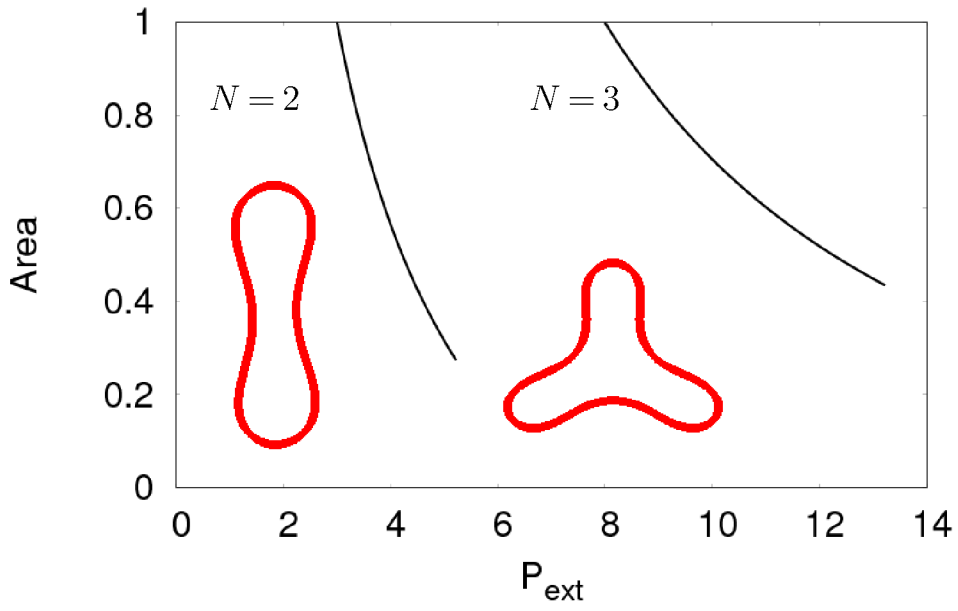

Figure 1. Buckling modes of a thin-walled elastic ring under uniform transmural pressure, P_{ext}, scaled by $Eh^3/(12R^3(1-\nu^2))$, quantified by enclosed area scaled by πR^2. A series of symmetry-breaking bifurcations is present, with each bifurcation corresponding to a different azimuthal mode number, N. The most unstable mode is $N = 2$, which is typically seen in experiments. These post-buckling curves are computed via finite-element solution of equation (2.1) under increasing constant external pressure load.

A closely related problem arises if the elastic ring is constrained by an outer rigid circular shell. This formulation of the problem is of relevance to applications ranging in size from the

confinement of polymer rings [11] to stability of underground pipelines [9] and the formation of spiral patterns in Nature by compression of elastic structures, see [12]. It is well-established that the situation is qualitatively different from the case of the free ring.

A very important result first shown by Chan & McMinn [13] is that the axisymmetric state remains stable for all values of compression. This result was confirmed in a combined numerical and analytical study using compression by point loads [14]. Specifically, the external constraint prevents decomposition of the deformation into standard Fourier modes (even an infinitesimal outward radial deformation is prevented by the presence of the ring), which means that equation (1.1) does not apply. Chan & McMinn [13,15] also highlighted the importance of imperfections in promoting the instability, which was later confirmed by numerical investigations [16]. The work was motivated by the buckling of steel rings inside pre-stressed concrete pressure vessels with applications in nuclear reactors. In this situation the compressive forces arise from the different coefficients of expansion of the two materials. It is now known that the stability of the axisymmetric solution is a robust phenomenon and is also present in rings of visco-elastic material [17].

Despite the theoretical predictions of stability of the unbuckled state, deformed states are frequently observed and a modified two-lobed mode can occur as a solution to the model equations. However, a finite perturbation is required to achieve it as shown in the finite element calculations [18] and complementary experiments [19], which included the effects of friction. In contrast to the unconstrained ring, the buckled state in the constrained problem does not arise at a pitchfork bifurcation from the circular state. Instead the branch corresponding to the buckled state is disconnected from the trivial branch and it is bounded by a saddle-node bifurcation i.e. a stable and unstable pair of branches meet at the saddle-node near the undeformed value of the radius.

This relatively simple system is a didactic example in which the base state is linearly stable, but there exists an alternative state that is observed in experiments under finite perturbation. In fact, Chan & McMinn showed that the buckled state becomes exponentially close to the base state as the radius of the confining ring decreases. Thus, eventually the imperfections in the system are enough to force the buckled state. The situation is not the same as the classic imperfection-sensitivity of thin-walled shells under pressure loading [20]. In this case, there are bifurcations from the trivial state, but the bifurcations are subcritical, which means that small imperfections can induce buckled states at much lower loads than in the perfect system. Despite these theoretical differences, however, the practical consequences will be the same and it would not be possible to identify the difference between the two solution structures from experiments alone.

In this paper we consider a series of novel constrained buckling problems in which the symmetry of the external confiner is modified from a continuous to discrete group. We replace the circle by a regular n-gon with $n > 2$. In this case we find that generically the system undergoes a buckling bifurcation at a critical level of confinement quantified by the radius of inscribed circle of the polygon. The instability has its origins in the classic column buckling of Euler [3] and the preferred mode is one in which the discrete symmetry of the polygon is retained after buckling. The critical radius for buckling increases with n and the polygon becomes more circular. Numerous alternative buckling modes can arise including a state analogous to the confined two-lobed mode in the circular system.

In addition, we conduct experimental investigation using a novel setup in which the elastic ring was steadily confined as water was removed in small drops from specially constructed funnels. The experimental results are in reasonable quantitative agreement with the theoretical model and demonstrate that the full-symmetry buckling mode occurs spontaneously but that other buckling modes require finite perturbation.

2. Methods

(a) Experiments

The experiments were conducted using latex rings of 1mm cross-section and internal radii of 36mm, giving $h/R = 1/36$. The latex rings were made by injecting a solution of the hyperelastic material extra hard Sid AD Special (Feguramed GmbH) into machined stainless steel moulds. The latex material was initially formed by mixing a degassed polyvinyl base and siloxane catalyst in the ratio of 1:1. While in the liquid state, the uniform mixture was injected into the stainless steel moulds and left to set for 30 minutes. The density of the rings was slightly greater than water at $\rho \approx 1,100 kgm^{-3}$, but the rings were kept afloat by surface tension. Preliminary experiments were also performed using rings of internal radii 18mm that were manufactured by injecting the latex material into a glass tube, breaking the tube and gluing the ends together. The resulting rings were tapered and had a visible bump at the join. The results from the 18mm rings, although qualitatively similar to those obtained using the 36mm rings, are quantitatively unreliable and for this reason we present data from experiments using the 36mm rings only.

The specially constructed funnels which contained the water were accurately fabricated from aluminium sheets. The water was removed from the funnel in millilitre drops using a calibrated pipette. The sheets forming the sides of the funnels were machined to size and silver soldered together while held on a machined former. The inner surfaces of the funnel were coated with Teflon to minimise frictional effects. The experimental setup is shown in Figure 2. As the water

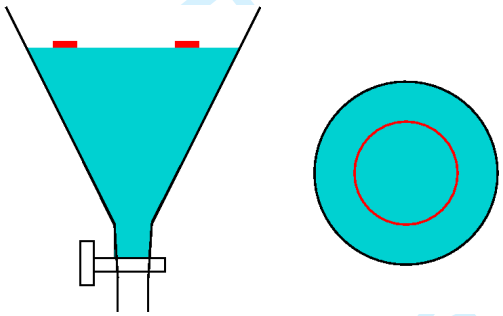

Figure 2. Schematic of the experimental setup: an elastic ring floats on the surface of water confined within a funnel of given cross-section.

was removed from the funnel, the water level dropped and the ring was constrained by the boundary. Images were taken by a top view camera and we used standard edge detection and image processing within Matlab to extract the surface area of the water enclosed by the ring for comparison with the numerical results. Typical overhead views are shown in Figure 3 for three different funnel shapes.

(b) Theoretical model

We are interested only in equilibrium configurations in which the fluid is at rest so we shall assume that the role of the fluid is purely passive in the sense that its presence ensures that a vertical force balance on the elastic ring is always maintained and that the ring remains planar. Thus, our model reduces to a problem in solid mechanics; however, the dynamic shape evolution during water drainage from the funnel presents a novel and challenging fluid-structure interaction.

The ring is assumed to an elastic beam of thickness h and undeformed radius R. Its deformation is described using geometrically non-linear beam theory [21]. Material lines normal to the undeformed centreline are assumed to remain unstretched and normal to the centreline during the deformation; hence, the position of the centreline is sufficient to describe the deformation of the beam. In a global Cartesian coordinate system, with origin at the centre of

the ring, the undeformed centreline is located at $\boldsymbol{R} = (R_1, R_2) = (R\cos\xi, R\sin\xi)$, parametrised by a single Lagrangian coordinate ξ that is equivalent to the polar angle. We assume that the strains induced by the deformation are sufficiently small to justify the use of an incrementally linear constitutive equation. Thus, the dimensionless second Piola–Kirchhoff stress is given by $\sigma = \sigma^*/E = \epsilon$, where E is the Young's modulus and ϵ is the Green–Lagrange centreline strain, see equation (2.2).

The principle of virtual displacements states that external work generated by the virtual displacement of an elastic body must be equal to the virtual change in its strain energy. Under the above assumptions the variational principle for ring takes the form

$$\int_0^{2\pi}\left[\epsilon\delta\epsilon + \frac{1}{12}\left(\frac{h}{R}\right)^2\kappa\delta\kappa\right]\mathrm{d}\xi = \frac{R}{h}\int_0^{2\pi}\boldsymbol{f}\cdot\delta\boldsymbol{R}\sqrt{\left(R_{1,\xi}\right)^2+\left(R_{2,\xi}\right)^2}\mathrm{d}\xi, \tag{2.1}$$

after analytic integration through the thickness of the beam. In the above, $R_{1,\xi} \equiv \partial R_1/\partial\xi$ and $R_{2,\xi} \equiv \partial R_2/\partial\xi$; the quantity ϵ is the Green–Lagrange centreline strain

$$\epsilon = \frac{1}{2}\left(\left|\frac{\partial\boldsymbol{R}}{\partial\xi}\right|^2 - 1\right) = \frac{1}{2}\left[\left(R_{1,\xi}\right)^2 + \left(R_{2,\xi}\right)^2 - 1\right]; \tag{2.2}$$

κ is the dimensionless change of curvature of the centreline

$$\kappa = \frac{R_{2,\xi\xi}R_{1,\xi} - R_{1,\xi\xi}R_{2,\xi}}{\sqrt{\left(R_{1,\xi}\right)^2+\left(R_{2,\xi}\right)^2}}; \tag{2.3}$$

and $\boldsymbol{f} = \boldsymbol{f}^*/E$ is the non-dimensional traction acting on the wall. Here, the first two terms in equation (2.1) represent the change in internal strain energy due to stretching and bending respectively and the final term is the work done by the external load acting on the deformed ring.

If we neglect gravitational and inertial effects, justified by an assumed small value of h/R (we used the experimental value of $h/R = 1/36$), then the load on the ring consists of the contribution from the presence of the funnel which in most cases is simulated by applying a large penalty pressure in the direction normal to the funnel wall:

$$\boldsymbol{f} = K_{wall}\frac{\boldsymbol{N}_{wall}}{|\boldsymbol{N}_{wall}|}\left(\frac{1}{d}\right)^4, \qquad d = \frac{|\boldsymbol{N}_{wall}|}{d_{crit}}. \tag{2.4}$$

In the above, $\boldsymbol{N}_{wall}$ is a vector from a given point on the ring to the nearest point on the wall in the normal direction of the wall but directed toward the ring and $|\boldsymbol{N}|$ denotes its length. Note that for polygonal funnels points on the ring may be equidistant from different straight-line sections of the wall, so contributions from all such sections of the wall are included. The parameters $K_{wall} = 0.1$ and $d_{crit} = 0.001$ were found to give contact regions that were within graphical accuracy, see the lower images in Figure 3. If these parameters are poorly chosen the ring will either penetrate the wall (penalty pressure too small) or be significantly displaced inwards (penalty pressure too large).

In order to assess the validity of this approach, however, we also imposed the solid contact exactly by introducing a contact pressure field $p_{contact}$ such that

$$\boldsymbol{f} = p_{contact}\,\boldsymbol{N}_{wall}.$$

The contact pressure is determined by using the constraint:

$$\begin{aligned} &\text{If } |\boldsymbol{N}_{wall}| > 0, \qquad p_{contact} = 0. \\ &\text{If } |\boldsymbol{N}_{wall}| \le 0, \qquad |\boldsymbol{N}_{wall}| = 0. \end{aligned} \tag{2.5}$$

In other words, the contact pressure is zero if the ring has not penetrated the wall, but if penetration has occurred then the ring is constrained to be exactly located on the wall and the associated contact pressure will be found to satisfy this constraint. The results for the two formulations are indistinguishable apart from near bifurcation points where the penalty method can act as an imperfection.

The variational principle is discretised using Hermite beam elements in which the positions are approximated by cubic polynomials within each element and continuity of position and its azimuthal gradient between elements is enforced. The contact pressure is discretised by linear shape functions and the contact constraint (2.5) is enforced by collation at each node. The discrete set of equations is assembled and solved using the finite element library `oomph-lib` [22]. The non-linear algebraic equations are solved using a globally convergent Newton method where each linear system is solved using a direct solver (SuperLU). Typically 300 elements are used to discretise the entire ring. If the entire ring is discretised then no particular symmetry is enforced, but the horizontal position of one degree of freedom is pinned to avoid translational degeneracy for large rings. In order to speed up calculations, we have also used alternative formulations in which specific symmetries are enforced to reduce the number of alternative conjugate solution branches. When examining the two-lobed buckling mode, we solve over half the ring enforcing a single reflection symmetry, but when examining the initial buckling instability we solve over $\frac{1}{2n}$-th of the ring with reflection symmetries imposed on two straight lines from the centre of the inscribed circle separated by an angle π/n. In these formulations the number of elements can be reduced.

Determining the stability of the confined rings is not straightforward owing to the presence of the unilateral contact constraints. This problem is obviated by using the penalty approach (2.4) in which the constraint is not applied exactly. However, if using a standard linear stability analysis eigenfunctions that violate the confinement must be rejected [23]. Pocheau & Roman [24] discuss the problem of multiplicity of solutions for an elastic strip contained within a box by developing non-local methods to find bifurcations. They find uniqueness of the solution until the regions of flat contact buckle in a classic Euler mode. More recently, an energy method was developed for stability analysis of such systems, which again relies on rejection of modes that violate the constraints [25].

In the following, we use a standard linear stability analysis and discard invalid modes, but used computational group theory to assess whether our methods for determining whether symmetry-breaking had occurred were robust [26]. The computer algebra system magma [27] was used to determine projection operators that could be applied to the full Jacobian matrix to extract reduced eigenvalue problems corresponding to whether a specific symmetry is broken. The method relies on knowing the symmetry group of the external container. In principle, the method can be used to reduce the computation time for stability calculations, but for the present problem the reductions in computation time were minimal and it was not used. Nevertheless, the method did confirm that the discrete system reproduced the appropriate symmetries and that the results of the stability analysis were identical when solving the full system or the set of reduced systems.

3. Results

Snapshots of typical experimental and simulation results for triangular, square and pentagonal containers are shown in Figure 4. It can be seen that the shapes obtained in the experiments and numerical simulations are qualitatively similar. The non-trivial (buckled) states all have the full symmetries of the bounding polygon. We can make a quantitative connection between the experiments and theoretical calculations by using the area enclosed by the ring to parametrise its shape and plot this against the area of the bounding shape. The results for the conical funnel (circular bounding shape) are shown in Figure 4. The trivial branch is shown as a dotted line and because the ring adopts the same shape as the funnel boundary (ignoring any meniscus effects) the branch is given by equality between both areas. The simulated disconnected buckled solution is shown as a solid line and the unstable region is almost indistinguishable from the circular state in the chosen measure. The stable buckled region is in good agreement with the experimental data, shown as black markers. The differences at higher compression arise because in the experiment the ring self-contacts and distorts into the third dimension. Typical unstable and stable buckled ring shapes are shown to demonstrate that the buckled region is extremely small

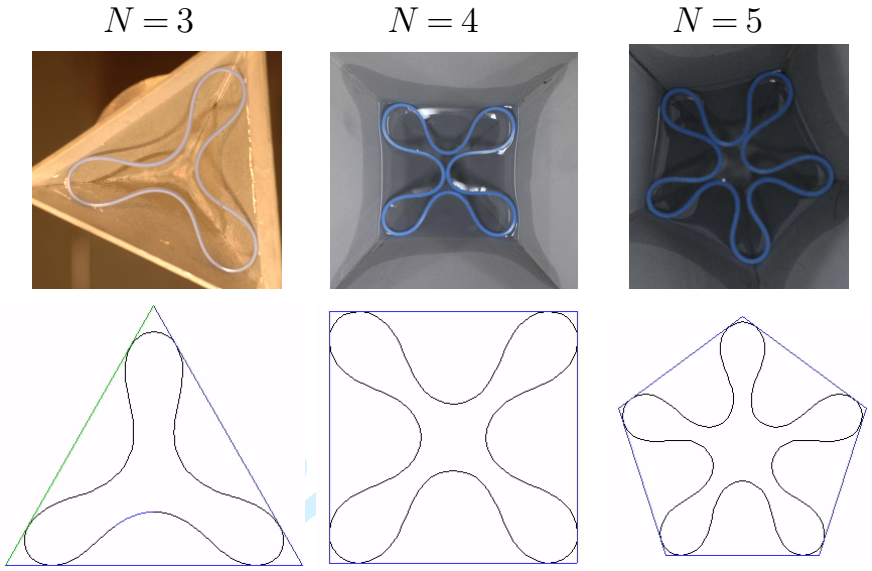

Figure 3. Overhead images from experiments and computations (using the penalty pressure formulation) in triangular, square and pentagonal containers for buckled shapes that maintain the discrete symmetry of the polygon. Note that the symmetry is approximate in the experimental images.

for the unstable buckled solution and more extensive for the corresponding stable solution. We also present additional computations using the Euler–Bernoulli beam model derived by Chann & McMinn [13] for the disconnected buckled branch, see the Appendix for details, which is in good agreement with the Kirchhoff–Love beam simulations and experimental data. Note that the larger enclosed area for the Chan & McMinn solution is due to the use of exact contact rather than a penalty pressure formulation. These results demonstrate that the novel experimental approach and theoretical model are both in line with the classical theory. Moreover, we confirm the finding that there is no bifurcation from the trivial axisymmetric solution.

For the funnels with polygonal cross-section, the solution structure is qualitatively different from the circular case. In these geometries, the trivial solution undergoes a buckling instability at a critical level of confinement. A comparison between experimental and theoretical results for the square funnel is shown in Figure 5. The comparison on the main branch (solid line and markers), which has the full symmetries of the square, is good except at large cross-sections, which may be due to meniscus effects forcing the ring to lie out of plane and therefore giving a smaller projected area. The buckling instability occurs at a surface area of approximately 3500 mm^2 and is indicated by the sharp change in gradient of the solution. Although linear stability analysis indicates that the main branch is unstable after buckling, inspection of the unstable modes reveals that they violate the confinement constraints and so must be discarded. Hence, we conclude that the branch is stable, as observed in the experiments. The agreement for the branch after finite perturbation is in less good quantitative agreement, but lies below the main branch in both cases. The experimental perturbation is imposed by displacing one of the sides and then releasing. Provided that the external compression is sufficient to induce buckling, then the chosen form of perturbation will cause the ring to "jump" into a post-buckled configuration similar to the one shown in Figure 5(f). Comparison with the closest simulation result, Figure 5(c), indicates that the experimental configuration is not perfectly symmetric and does not penetrate as far into the upper corners of the square cross-section, leading to a smaller enclosed area. We attribute this latter difference to the presence of the fluid meniscus which will rise more in the corners of the

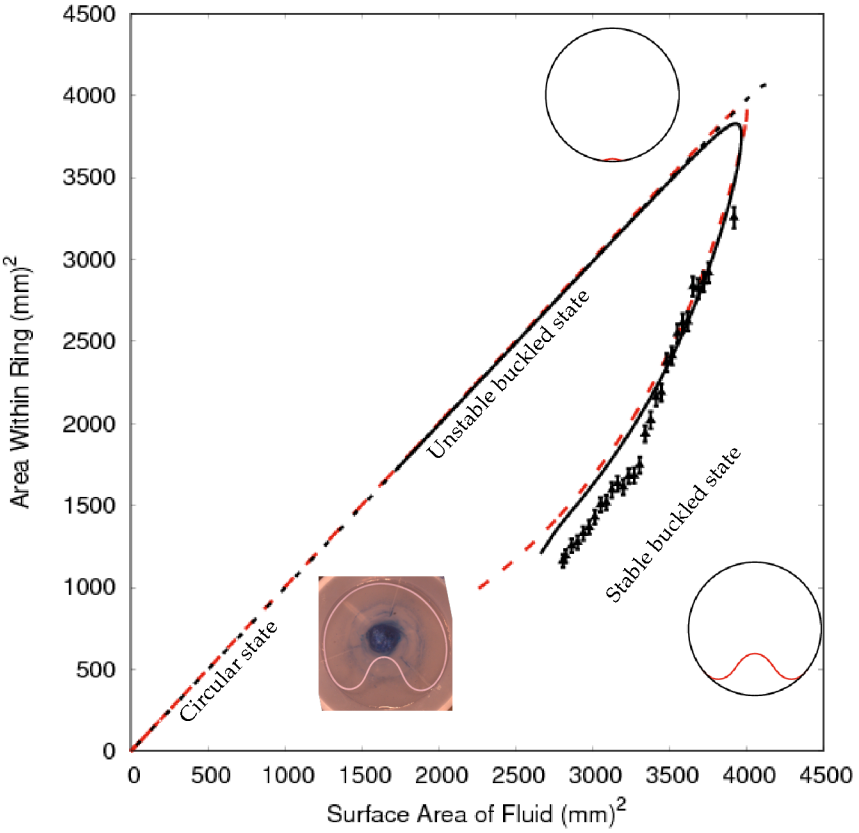

Figure 4. Compression in a conical funnel with circular cross section. Experimental data for buckled state is shown as black markers. Simulation results for the penalty pressure formulation are shown for the trivial branch (dotted black line) and the buckled solution (solid black line). The dashed (red) line shows results using the Euler–Bernoulli beam model developed by Chan & McMinn (1966a). The buckled solutions from the Chan & McMinn model are shown for a fluid area of 3868 mm^2. The unstable solution contains a small region of buckling, whereas the stable solution has a significant buckle. An experimental image for fluid area of 3756 mm^2 is also shown.

square funnel than along the edges; a difference that is not present in the conical funnel. The results for the triangular and pentagonal funnels are similar and therefore not reported. Note that the slight differences between the two simulations for larger fluid areas is because the main branch is computed using exact contact conditions, whereas the other branch was computed using a penalty pressure, which smooths out the change in gradient at bifurcation, acting as an imperfection, and leads to slightly smaller enclosed areas.

In order to understand the observed buckling, we remark that the system is no longer axisymmetric but has the symmetry of the bounding polygon and, crucially, the ring does not contact the entire polygon. Instead, for an n-gon the ring first makes contact at n points, which then develop into regions of line contact, as found when a plane wall compresses a bent elastic strip [28]. Indeed, it can be proved that for an Euler–Bernoulli elastica regions of line contact are inevitable under geometric compression [24]. These flat-contact regions behave like clamped Euler–Bernoulli beams which are unstable to buckling when $T > 4E\pi h^2/(12L^2)$, where T is the tension and L is the length of the beam. Increasing confinement of the ring means that the tension increases and also that the regions of line contact increase, increasing T and L. Thus, we expect the flat contact regions to buckle at a critical value of confinement, as confirmed in the experiments in polygonal funnels, see Figures 3, 5.

We note that because each region of line contact acts as an identical Euler column then many possible solutions can arise in the full problem because all, some or none of the line contact regions could buckle at the same critical level of confinement. As expected from equivariant bifurcation theory [29] many of these solutions are conjugate under rotation or reflection. However, states other than the buckled solution with full symmetry require finite perturbations to achieve

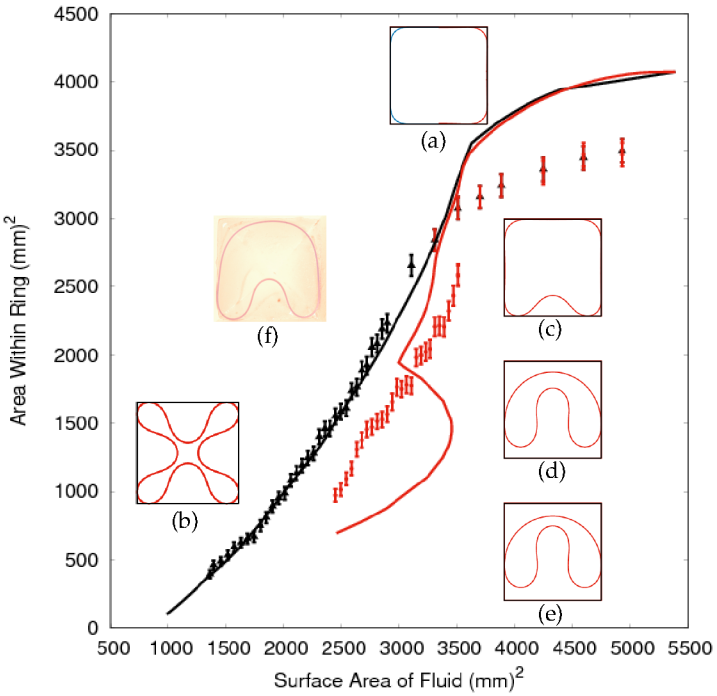

Figure 5. Comparison of experimental data (markers) on the main (full-symmetry) branch (large black triangles) and after finite perturbation (small red triangles) against model predictions (solid lines) for the main branch (black) and a two-lobed post-buckling branch (red) in a square funnel. Simulation results are shown on the main branch for (a) unbuckled state at fluid area of 3675 mm^2, the right-hand side corresponds to the penalty pressure approach and the left-hand side corresponds to exact contact; and (b) buckled mode with full symmetry at a fluid area of 1654 mm^2. On the finite perturbation branch (c), (d), (e) correspond to buckled states with single reflection symmetry at the same fluid area of 3443 mm^2. An experimental image is shown on the finite perturbation branch (f) corresponding to a fluid area of 3430 mm^2.

experimentally. This is consistent with these branches being subcritical at buckling and then being stabilised by a subsequent saddle-node bifurcation. Consequently, there are (at least) two possible post-buckled solutions for the same degree of confinement as already found in the circular problem, see Figure 4 and observed in the buckling of a single strip contained in a box [24].

Interpretation via Euler–Bernoulli theory

We can predict the value of confinement required to cause buckling by appealing to the classic Euler–Bernoulli elastica model used by the majority of previous studies in this area, see Howell *et al.* [30] §4.9 for a derivation. The tension in the beam $\boldsymbol{T}(s) = P(s)\boldsymbol{e}_x + Q(s)\boldsymbol{e}_y$ where $\boldsymbol{e}_x$ and $\boldsymbol{e}_y$ are the base vectors of a global Cartesian coordinate system and s is the arclength measured along the beam. Assuming a linear constitutive law relating the bending moment to curvature then equilibrium of moments and forces over a section of the beam yields the classic equations for a beam with square cross-section of thickness h:

$$\frac{Eh^4}{12}\frac{\partial^2\theta(s)}{\partial s^2} = -P(s)\sin\theta + Q(s)\cos\theta, \quad \frac{\partial P(s)}{\partial s} = F_x(s), \quad \frac{\partial Q(s)}{\partial s} = F_y(s), \tag{3.1}$$

where $\theta(s)$ is the angle formed between the x-axis and the beam; and $\boldsymbol{F}(s) = F_x(s)\boldsymbol{e}_x + F_y(s)\boldsymbol{e}_y$ is the external load. We note that the equations that result from considering an initially curved ring and an initially straight beam bent into a ring shape are identical [15]. Thus, we can indeed appeal to the results of conventional beam theory. Once θ is known the x and y positions along the beam can be found by integrating the defining equations

$$\frac{\partial x}{\partial s} = \cos\theta, \qquad \frac{\partial y}{\partial s} = \sin\theta. \tag{3.2}$$

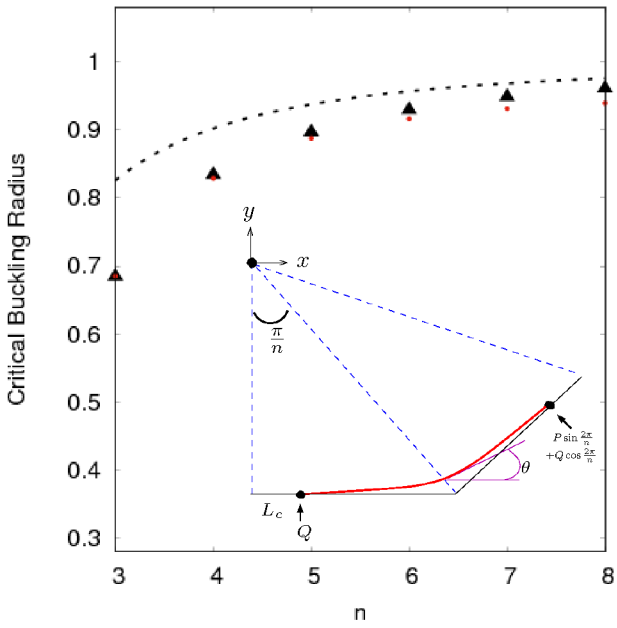

Figure 6. Critical buckling radius of the inscribed circle for a regular n-gon relative to the undeformed radius of the ring (r_{crit}/R) for an inextensible Euler–Bernoulli model (large markers) and the Kirchhoff–Love model (small dots). The asymptotic approximation, equation (3.6), for the critical load in the Euler–Bernoulli model is shown as a dotted line. Inset: Sketch of geometry for Euler–Bernoulli model. The equation (3.1) is solved between two regions of flat contact, subject to an overall length constraint. Contact forces are determined as part of the solution.

In order to determine the critical buckling load in a regular polygonal container we consider the fully symmetric case and model $1/n$-th of the domain so that θ takes the values from 0 to $2\pi/n$, see inset in Figure 6. We assume that a region of the beam is in flat contact with the bounding walls and that the equations (3.1) are solved between flat contacts. The boundary conditions are that $\theta = 0$ at the left-hand contact point and $\theta = 2\pi/n$ at the right-hand contact point. In between the contact points there is no external force applied to the beam, which means that P and Q are both constant after integrating the force balance equations in (3.1). At both contact points the curvature is zero so $\frac{\partial\theta}{\partial s} = 0$, which we use as constraints to determine the unknown contact pressures P and Q. The y value at the left-hand boundary is simply $y = -r$, where r is the radius of the largest inscribed circle within the bounding polygon. For simplicity we assume that the elastica is inextensible of length $2\pi R/n$ so that $2\pi R/n = 2L_c + L$, where L is the length of the non-flat region, which is a constraint used to determine the unknown contact position L_c. Finally the unknown length L is determined by the constraint that the right-hand boundary must lie on

the neighbouring boundary of the polygon: a line defined by

$$y = \tan(2\pi/n)x - r\left[1 + \tan(2\pi/n)\tan(\pi/n)\right]. \tag{3.3}$$

We discretise and solve the equations (3.1) using quadratic finite elements via the library `oomph-lib` and report the critical buckling radii of the inscribed circles in Figure 6 as black markers. The Figure also shows red dots corresponding to the critical loads computed by numerical linear stability analysis of the Kirchhoff–Love beam model (2.1) discretised over $1/(2n)$-th of the full domain. A greater confinement (smaller radius) is required to induce buckling in the Kirchhoff–Love beam because it is not inextensible and will initially compress before buckling to accommodate the elevated tension. The deviation between the two models increases with increasing n because the tension in the ring (and hence the level of compression) increases with n. Figure 6 further demonstrates that less confinement is required to induce buckling as n increases. In other words for polygons with increasing number of sides the buckling instability occurs when the radius of the inscribed circle is greater. The same general trend is found in the experiments, but the critical buckling radius cannot be determined to sufficient accuracy to provide a reliable quantitative comparison with the theoretical data. An analytic prediction for the critical buckling radius of the Euler–Bernoulli beam is also shown on Figure 6 and is consistent with the computations.

This analytic prediction is possible because the equation for θ can be simplified by using the symmetry requirement that $P = F\cos(\pi/n)$ and $Q = F\sin(\pi/n)$ for some scalar F, which ensures that the tension is normal to the symmetry line between the two sides of the polygon. Hence the equation for θ becomes

$$\frac{\partial^2\theta}{\partial s^2} = -\hat{F}\cos(\pi/n)\sin\theta + \hat{F}\sin(\pi/n)\cos\theta = F\sin\left(\pi/n - \theta\right), \tag{3.4}$$

where $\hat{F} = 12F/(Eh^4)$. We know that θ takes values between 0 and $2\pi/n$ and hence for sufficiently large n, θ will remain small and we can linearise (3.4) to obtain

$$\frac{\partial^2\theta}{\partial s^2} = \hat{F}\left[\frac{\pi}{n} - \theta\right].$$

We use the boundary conditions for θ and $\partial\theta/\partial s$ to obtain the solution

$$\theta = \frac{\pi}{n}\left(1 - \cos\pi\hat{s}\right), \tag{3.5}$$

where $\hat{s} = s/L$ is a scaled arclength coordinate. Note that the value of $\hat{F}$ is an eigenvalue and we have chosen the mode with the least bending, in which case $\hat{F}L^2 = \pi^2$. Comparison with the finite element solution shows that this is actually a very good approximation for all $n > 2$.

We proceed by integrating the equations

$$\frac{\partial x}{\partial\hat{s}} = L\cos\theta \approx L\left(1 - \frac{\theta^2}{2}\right) \quad \text{and} \quad \frac{\partial y}{\partial\hat{s}} = L\sin\theta \approx L\theta,$$

to obtain

$$x = L\left[\left(1 - \frac{3\pi^2}{4n^2}\right)\hat{s} + \frac{\pi}{n^2}\sin\pi\hat{s} - \frac{\pi}{2n^2}\sin 2\pi\hat{s}\right] + L_c,$$

$$y = \frac{L}{n}\left(\pi\hat{s} - \sin\pi\hat{s}\right) - r,$$

after using the boundary conditions for x and y at $\hat{s} = 0$.

We still have two unknown lengths L and L_c, but we have two constraints to enforce: (i) at $\hat{s} = 1$ the beam must lie on the line defined by equation (3.3); and (ii) the total length of the beam is known from inextensibility, $2L_c + L = 2\pi R/n$. Note that the left-hand side of this constraint does not take into account the error in length due to the approximations for $\cos\theta$ and $\sin\theta$ used to find x and y, which are, in fact, the largest sources of error in this approximation. These two

constraints can be used to determine L_c and L and we find that

$$L = \frac{\left(\frac{\pi R}{n} - r\tan(\pi/n)\right)\tan(2\pi/n)}{\frac{\pi}{n} - \frac{1}{2}\left(1 - \frac{3\pi^2}{2n^2}\right)\tan(2\pi/n)}, \quad \text{and} \quad L_c = \frac{\pi R}{n} - \frac{L}{2}.$$

In the limit $n \to \infty$ we find that $L \to 4n(R-r)/3$, which only makes sense if the allowed solutions for increasing n have $(R-r) \to 0$ faster than $n \to \infty$. We use this approximation to determine the critical buckling radius as a function of n. An Euler–Bernoulli beam of length $2L_c$ will buckle when the applied load (scaled by $Eh^4/12$) exceeds $\frac{\pi^2}{L_c^2}$. Hence, $\hat{F}\cos(\pi/n) > \pi^2/L_c^2$, but $\hat{F} = \pi^2/L^2$ from above and so at the critical level of confinement, assuming that $\cos(\pi/n) \approx 1$, $L^2 \approx L_c^2$, which means that $L \approx L_c$ and so from the inextensibility constraint $L \approx \frac{2\pi R}{3n}$. Thus as $n \to \infty$,

$$\frac{4n(R - r_{crit})}{3} \approx \frac{2\pi R}{3n} \quad \Rightarrow \quad \frac{r_{crit}}{R} \approx 1 - \frac{\pi}{2n^2}. \tag{3.6}$$

Note that a more accurate formula could be derived by relaxing the approximations made when determining x and y, but our main purpose in this analysis is to demonstrate that $r_{crit}/R \to 1$ as $n \to \infty$, indicating that the critical radius of the inscribed circle approaches the undeformed radius of the ring.

4. Conclusions

In this paper we have demonstrated that there is a qualitative difference between constrained buckling of an elastic ring when the confining geometry changes from circular to polygonal. In the former, the (axisymmetric) solution with full symmetry of the system is always linearly stable and the buckled solutions are all disconnected from the main branch. Consequently a finite perturbation is required to induce buckling. In the latter, the ring cannot remain axisymmetric and regions of point and then line contact develop along the polygonal walls. The line contact regions are effectively Euler columns and will buckle when the tension in the ring is sufficiently high. Thus, in polygonal geometries the buckled solutions are connected to the main branch via a bifurcation and buckling can occur under infinitesimal perturbations. Indeed, different buckling modes are possible all arising from the same bifurcation point because each individual line-contact region may or may not buckle. Experimentally, the post-buckled solution in which the full discrete symmetry of the system is preserved is favoured and finite perturbations are required to reach the other modes.

As the number of sides of the polygon increases, the critical radius of the inscribed circle within the polygon required to induce buckling tends towards the undeformed radius of the elastic ring, but it will always be present. Thus, the polygonal boundary is always fundamentally different from the circle. However, the mechanism identified in the present paper could occur in circular containers with localised geometric imperfections that lead to flattening of the boundary. If the ring can be placed into flat line contact along a region of the boundary (no matter how small) then it will eventually buckle there. Indeed, such localised geometric imperfections could provide the required finite perturbation to induce the well-known disconnected buckling modes.

5. Appendix

In order to determine the post-buckled solutions for the circular container we follow [13] and solve the Euler–Bernoulli equations (3.1) between two contact points assumed to lie symmetrically about the lowest point of the circle. The angles corresponding to these points in a polar coordinate system with origin at the centre of the circle are $\pm\alpha$. We therefore solve a

rescaled version of the equations in one half of the domain

$$\frac{\partial^2\theta(\hat{s})}{\partial\hat{s}^2} = L^2\left[-\hat{P}(s)\sin\theta + \hat{Q}(s)\cos\theta\right], \quad \frac{\partial x}{\partial\hat{s}} = L\cos\theta, \qquad \frac{\partial y}{\partial\hat{s}} = L\sin\theta, \tag{5.1}$$

where L is the unknown (half-)length of the buckled region, $\hat{s}\in[0,1]$ is a scaled arclength coordinate, and $\hat{P} = P/((Eh^4)/12))$ and $\hat{Q} = Q/((Eh^4)/12))$ are dimensionless components of the tension. We choose a global Cartesian coordinate system with origin at the centre of the circle.

The boundary conditions are that on the symmetry line ($s=0$) $\theta = 0$ and $x = 0$; whereas at the contact point ($s=1$) $\theta = \alpha$ and $y = -r\cos\alpha$, where r is the radius of the bounding circle. The values $\hat{P}$ and $\hat{Q}$ are constant from the equilibrium of forces, but their values are unknown, as is the length L. In order to determine the unknown tension components we use the facts that the curvature of the beam must match the curvature at the contact point: $\partial\theta/\partial\hat{s} = L/r$ at $s=1$; and that the symmetry condition at $s=0$ means that the vertical component of the tension must be zero. (Note that it is easier to locate the buckled solution branch numerically if the vertical position of the beam at $s=0$ is treated as an additional unknown Y with the associated equation that $Q=0$.) The unknown length L is found from the constraint that at $s=1$, $x = r\sin\alpha$. Solving this set of equations and constraints using quadratic finite elements via `oomph-lib` we find a post-buckled solution for given α if we insist that $Y > -r$.

In order to link this constructed solution to the undeformed ring we treat α as an unknown with the constraint that the length change due to axial strain induced by the tension (assuming a linear constitutive law) is consistent with the actual length of the buckled solution. Under the assumption that the region in contact with the outer circle is uniformly strained we obtain:

$$2\pi R - \hat{P}\frac{h^2}{12R^2}\left[2(\pi-\alpha)\cos\alpha - 2\sin\alpha\right]R = 2r(\pi-\alpha) + 2L, \tag{5.2}$$

where the left-hand side is the length that follows from the imposed tension $P\boldsymbol{e}_x$ and the right-hand side is the total length of the solution. The final term on the left-hand side follows on integrating the axial tension over the buckled region, which yields the difference in x-coordinates of the end points multiplied by the component $\hat{P}$. The complete solution branch is then determined by using arclength continuation. Note that equation (5.2) is the only point in the calculation when h/R enters explicitly, as one might expect because it is the only equation in which axial strain and bending are related. In our calculations we used the value $h/R = 1/36$, but we note that as $h/R\to 0$ and the ring tends towards the inextensible limit, the location of the saddle-node bifurcation approaches the undeformed radius ($r_{saddle\text{-}node}\to R$), suggesting a potential connection with the polygonal limit $n\to\infty$ found above.

Data Accessibility. All supporting data is provided within the manuscript.

Authors' Contributions. TM performed the experiments and data analysis. AH developed the theory and performed the numerical simulations. The study was conceived and designed by both authors. The paper was drafted by both authors.

Acknowledgements. This work was initiated while TM was visiting ESPCI (Paris). We would like to thank Jose Bico for help at the start of the project. The computational group theory work was performed by John Ballantyne and Peter Rowley at The University of Manchester and supported by funds from EPSRC via the MAPLE Platform grant EP/I01912X/1. We would also like to thank Matthias Heil, Anne Juel, Chris Johnson, Nico Bergemann and Edgar Häner for helpful discussions.

References

1. Flaherty JE, Keller JB, Rubinow SI. 1971 Post buckling behavior of elastic tubes and rings with opposite sides in contact.
SIAM J. Appl. Math. **23**, 446–455.
2. Vasilikis D, AKaramanos S. 2014 Mechanics of confined thin-walled cylinders subjected to external pressure.
App. Mech. Revs. **66**, 010801.

3. Euler L. 1778 Die altitudine colomnarum sub proprio pondere corruentium. *Acta Acad. Sci. Imp. Pet.* **1**, 163–193.
4. Timoshenko SP, Gere JM. 1961 *Theory of Elastic Stability. Second Edition*. McGraw-Hill.
5. Mouthuy PO, Coulombier M, Pardoen T, Raskin JP, Jones AM. 2012 Overcurvature describes the buckling and folding of rings from curved origami to foldable tents. *Nature Comm.* **231**, 1290.
6. Gibson LJ. 2005 Biomechanics of cellular solids. *Journal of Biomechanics* **38**, 377–399.
7. M Heil M, Hazel AL. 2011 Fluid-structure interaction in internal physiological flows. *Ann. Rev. Fluid Mechs.* **43**, 141–62.
8. Lauga E. 2016 Bacterial hydrodynamics. *Ann. Rev. Fluid Mech.* **48**, 105–130.
9. Omara AM, Guice LK, Straughan WT, Akl FA. 1997 Buckling models of thin circular pipes encased in rigid cavity. *J. Eng. Mech.* **123**, 1294–1301.
10. Putelat T, Triantafyllidis N. 2014 Dynamic stability of externally pressurized elastic rings subjected to high rates of loading. *Int. J. of Solids and Struct.* **51**, 1–12.
11. Ostermeir K, Alim K, Frey I. 2010 Buckling of stiff polymer rings in weak spherical confinement. *Phys. Rev. E* **81**, 061802.
12. Boué L, Adda-Bedia M, Boudaoud A, Cassani D, Couder Y, Eddi A, Trejo M. 2006 Spiral patterns in the packing of flexible structures. *Phys. Rev. Lett.* **97**, 166104.
13. Chan HC, McMinn SJ. 1966 The stability of a uniformly compressed ring surrounded by a rigid surface. *Int. J. Mech. Sci.* **8**, 433–442.
14. Bottega WJ. 1988 On the constrained elastic ring. *J. Eng. Math.* **22**, 43–51.
15. Chan HC, McMinn SJ. 1966 The stabilisation of the steel liner of a prestressed concrete pressure vessel. *Nuc. Eng. and Des.* **3**, 66–73.
16. Kyriakides S, Youn SK. 1984 On the collapse of circular confined rings unde external pressure. *Int. J. Sol. Struct.* **26**, 699–713.
17. Yang M, Xiao SF. 2011 Confined buckling analyis of a viscoelastic ring subjected to constant temperature difference. *Adv. Mat. Res.* **295**, 1804–1810.
18. Sun C, Swan WDJ, Vinogradov AM. 1995 Instability of confined rings: An experimental approach. *Exp. Mech.* **35**, 97–103.
19. Sun C, Swan WDJ, Vinogradov AM. 1995 Discrete-element model for buckling analysis of thin ring confined within rigid boundary. *J. Eng. Mech.* **121**, 71–79.
20. Hutchinson JW. 1967 Imperfection sensitivity of externally pressurized spherical shells. *J. Appl. Mech.* **34**, 49–55.
21. Wempner GA. 1973 *Mechanics of solids*. New York: McGraw–Hill.
22. Heil M, Hazel AL. 2006 `oomph-lib` – an object-oriented multi-physics finite-element library. In *Fluid-Structure Interaction* (ed. M Schäfer, HJ Bungartz), pp. 19–49. Springer. `oomph-lib` is available as open-source software at `http://www.oomph-lib.org`
23. Ro WC, Chen JS, Hong SY. 2010 Vibration and stability of a constrained elastica with variable length. *Int. J. of Solids and Struct.* **47**, 2143–2154.
24. Pocheau A, Roman B. 2004 Uniqueness of solutions for constrained elastica. *Physica D* **192**, 161–186.
25. Chen JS, Lu CJ, Lee CY. 2015 On the use of energy method with element splitting to determine the stability of constrained elastica. *Int. J. of Non-Linear Mechanics* **76**.

26. Matthews P. 2004 Automating symmetry-breaking calculations. *LMS Journal of Computation and Mathematics* **7**, 101–119.
27. Bosma W, Cannon J, Playoust C. 1997 The Magma algebra system. I. The user language. *J. Symbolic Comput.* **24**, 235–265. (doi:{10.1006/jsco.1996.0125}.\newblockComputationalalgebraandnumbertheory(London, 1993
28. Plaut RH, Suherman S, Dillard DA, Williams BE, Watson LT. 1999 Deflections and buckling of a bent elastica in contact with a flat surface. *Int. J. Solids & Structures* **36**, 1209–1229.
29. Golubitsky M, Stewart IN, Schaeffer DG. 1988 *Singularities and Groups in Bifurcation Theory*. Springer-Verlag (Berlin).
30. Howell P, Kozyreff G, Ockendon J. 2009 *Applied Solid Mechanics*. Cambridge University Press.

Tran